

# Visiflex: A Low-Cost Compliant Tactile Fingertip for Force, Torque, and Contact Sensing

Alfonso J. Fernandez, Huan Weng, Paul B. Umbanhowar, and Kevin M. Lynch

**Abstract**—We present the Visiflex, an inexpensive compliant tactile fingertip capable of contact localization and 6 degree-of-freedom (dof) contact force and torque measurement. Because manipulation of rigid or nearly-rigid objects requires compliance at the contact, we build compliance directly into the Visiflex in the form of a well-characterized 6-dof flexure between the fingertip and the base of the Visiflex. This compliance also allows the use of a 6-dof position sensor to measure forces and torques transmitted through the fingertip. The position sensor is a camera, and the same camera is used to detect contact locations on the fingertip via frustrated total internal reflection (FTIR). Our tests indicate that typical errors in contact location detection are less than 1 mm and typical errors in force sensing are less than 0.3 N. A video of the Visiflex can be found online<sup>1</sup>.

**Index Terms**—Force and Tactile Sensing, Dexterous Manipulation, Grasping

## I. INTRODUCTION

MANIPULATION of rigid or nearly rigid objects often requires compliance at the manipulator. This compliance can come from any of several sources, including active compliance or impedance control; intentional mechanical design using passive springs, soft materials, series-elastic actuators, or variable stiffness or impedance actuators; and unavoidable compliance in links and joints with finite stiffness.

In our previous work on in-hand manipulation [1, 2], we showed that *spring-sliding compliance* enables regrasp of an object by sliding it within a grasp. Spring compliance ensures that fingers remain in contact while sliding over general surfaces, while sliding acts as a type of nonlinear damping “compliance” governing the relationship between tangential frictional forces and tangential sliding velocities. The method for achieving in-hand sliding regrasp described in [2] applies to objects of arbitrary three-dimensional geometries and a wide variety of multi-fingered robot hands, but the general approach requires fingertips with the following properties: (1)

Manuscript received: October 15, 2020; Revised January 12, 2021; Accepted February 3, 2021. This paper was recommended for publication by Editor Dan Popa upon evaluation of the Associate Editor and Reviewers’ comments. (Corresponding author: Alfonso J. Fernandez.)

This work was supported by NSF IIS-1952598.

The authors are with the Center for Robotics and Biosystems and the Department of Mechanical Engineering, Northwestern University, Evanston, IL 60208 USA. Kevin M. Lynch is also affiliated with the Northwestern Institute on Complex Systems (NICO). (emails: alfonsofernandez2017@u.northwestern.edu, huanweng@u.northwestern.edu, umbanhowar@northwestern.edu, kmlynch@northwestern.edu). We thank Jiarui Li, Chris Tsai-Tsao, Joshua Werblin, Hannah Russell, Peter Hartman, Yujie Jiang, Yuqiu Huang, and Ryan Fong for their contributions to design, experiments, and software, and Bill Strong for his expertise in manufacturing.

Digital Object Identifier (DOI): see top of this page.

<sup>1</sup><https://youtu.be/A9izoUP8BtE>

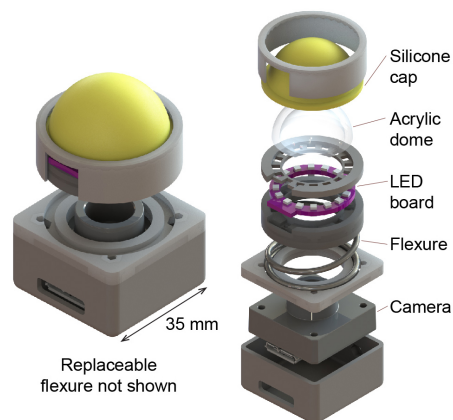


Fig. 1: (Left) A rendering of the Visiflex without the 6-dof flexure connecting the base and the fingertip. The flexure can be changed to fit the specifications of the application. (Right) An exploded view of the Visiflex, where a compression spring is used as the 6-dof flexure element. Missing from the figure is the opaque Lycra shroud between the base and the fingertip that blocks external light.

well characterized (or controlled) stiffness; (2) contact location sensing; and (3) contact force sensing. Further, the fingertip hardware should be relatively inexpensive, so it can be used on multiple fingers without being cost prohibitive.

Commercially-available tactile sensors do not meet these criteria, and the performance of closed-loop compliance control of robot fingers, relative to passive mechanical compliance, can be degraded by friction, backlash, and limited servo rates. For these reasons, we developed a compliant tactile fingertip combining (1)-(3), incorporating well-characterized mechanical compliance into the fingertip, so the fingertip could be used on a variety of robot hands, including those capable of position control but not well suited for stiffness control. We call this compliant tactile fingertip the *Visiflex*.

The Visiflex is illustrated in Figure 1. It consists of a hemispherical fingertip connected by a 6-dof flexure to a base. This modular design allows the flexure to be swapped out as needed for the application. For example, a stiffer flexure could be used on robot hands with stronger fingers for applications with higher maximum forces.

A camera in the base of the Visiflex tracks fiducials on the fingertip to reconstruct the fingertip’s 3D position and orientation. From this information, and the known flexure stiffness, the wrench (force and torque) applied through the

fingertip is determined.

The fingertip consists of a dome-shaped acrylic waveguide covered by a silicone cap. LED light injected into the waveguide is totally internally reflected except where the cap contacts the waveguide. Any contact results in FTIR, scattering light back to the camera in the base, which recognizes this as contact on the fingertip. Thus the same camera is used for multi-contact localization and wrench sensing.

The Visiflex prototype is capable of 40 Hz sensing of contact locations with an accuracy of 1 mm or better (typical) and contact forces with a typical accuracy of 0.3 N. The compliance of the sensor and its relatively low update rate make it appropriate for tactile feedback during quasistatic manipulation, such as the spring-sliding regrasps of [2], but not for fast dynamic manipulation.

The rest of this paper is structured as follows. Section II explores related work in the fields of tactile sensing and compliant mechanism development. Section III describes the mechanical design of the device in greater detail. Vision processing is described in Section IV, and the performance of the sensor is measured in Section V.

## II. RELATED WORK

### A. Tactile Sensing

Many tactile sensors are designed based on arrays to allow spatial resolution of contacts. For example, array-based tactile sensors have employed capacitive [3, 4, 5], resistive [4], magnetic [6], piezoelectric [7], and fiber Bragg grating [8] sensing technologies, among many others. A significant challenge is achieving a high density of sensors (“taxels”) and the wiring needed to address the taxels. The challenges of constructing arrays of taxels are discussed in many review papers on tactile sensing, e.g., [9, 10].

Cameras efficiently solve the problem of addressing millions of individual sensors (pixels) at rates of 60 Hz or more, so some tactile sensors have been constructed by converting touch signals to optical signals [11]. Maekawa et al. [12, 13] used an optical waveguide mechanism and a camera or position-sensitive detector to detect contact, similar to the Visiflex. More recent camera-based tactile sensors include the Tac-Tip [14], which uses a camera to detect displacements of pins embedded in a soft skin; FingerVision [15], in which cameras view the world through transparent skin with embedded markers, allowing the cameras to see objects before contact and to see the shear of the skin through the motion of the markers; and the GelSight [16], which is capable of detecting local shear forces and resolving the fine details of the shape of a surface. The DIGIT sensor [17] builds on the GelSight concept by reducing the overall sensor size, increasing the durability of the gel, and re-designing for large-scale production. The OmniTact [18] uses five cameras in a single sensor to achieve multi-directional contact and force detection, with the assistance of machine learning to interpret the sensor data.

Other optical approaches to tactile sensing rely on discrete LEDs and photoreceptors, such as the force sensor of Tar and Cserey [19], which eventually became the OptoForce force

sensor, and the recent work of Piacenza et al. [20], which embeds pairs of color LEDs and photodiodes in an elastomer skin. LED light traveling through the elastomer is received at the photodiodes in different ways, depending on the locations and forces at contacts on the skin, and the mappings between photodiode signals and contact locations and forces are learned using neural networks.

Two recent papers describing tactile or wrench sensors merit particular mention: the flexure-based force-torque sensor of Ouyang and Howe [21] and the F-TOUCH tactile sensor [22]. The F-TOUCH extends the GelSight concept by mounting the flat tactile surface on springs embedded in elastomer. The same camera implementing GelSight functionality also measures the displacement of markers to estimate forces and torques based on a fitted stiffness matrix. The force-torque sensor of [21] uses a camera to observe the displacement of tags on a platform supported by four compression springs. A linear transformation converts these displacements to forces and torques.

As with the Visiflex, both sensors employ flexures and visual estimation of displacements to estimate wrenches. A few differences among the sensors include the following. The sensor in [21] is a force-torque sensor only, not a contact or tactile sensor. The sensor of [21] and the Visiflex rely solely on metallic flexures for superior hysteresis and stress relaxation properties, whereas the F-TOUCH flexure includes an elastomer.

The F-TOUCH employs a mapping from visual displacements directly to wrenches, without separately estimating the rigid displacement of the fingertip, as in the Visiflex. This displacement is important to determine contact locations in space, and we characterize the accuracy of fingertip displacement sensing using a highly accurate multi-axis positioning device (the LIPMM, Section V-A). The F-TOUCH uses a GelSight-like flat sensing surface, appropriate for palmar-type manipulation or determining fine surface details, while the Visiflex has a hemispherical shape intended to allow rolling contact in robot manipulation.

### B. Flexure Design

Material properties and geometry play dominant roles in the multi-dimensional stiffness properties of a flexure [23]. When purely elastic properties are desired, as well as low hysteresis, stress relaxation, and creep, metals typically offer superior performance to other materials ([24, 25]), though rubber can also offer relatively low hysteresis while allowing large deformations [26]. For ease of manufacturing, easily-molded or 3D-printed materials, including thermoplastic polymers and photopolymers, have been used to design flexible structures with tunable properties (e.g., [27]), but these materials typically exhibit non-ideal material properties such as significant hysteresis and stress relaxation.

Hopkins and Culpepper created a systematic design method called Freedom and Constraint Topologies (FACT) [28, 29], in which a library of topologies with different degrees of freedom is provided as a design tool. Howell et al. outline several methods for the design of the geometry and topology of compliant

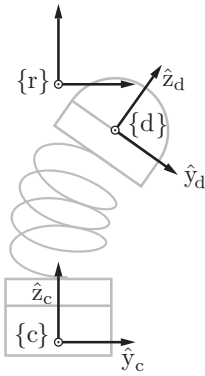


Fig. 2: The camera frame  $\{c\}$ , the fingertip dome frame  $\{d\}$ , and the frame  $\{r\}$  corresponding to  $\{d\}$  when the flexure is relaxed, i.e., no wrench is applied to the fingertip.

mechanisms to meet required specifications [23, 30]. One technique, the pseudo-rigid-body model, simplifies the analysis of mechanisms by approximating the continuous deformation of a flexure as localized [25, 31]. Topology optimization is another approach to flexure design, where material is virtually “whittled away” from a block of material until the resulting flexure displays the desired input-output force-displacement properties (e.g., [32, 33, 34]). Other approaches to flexure design can be found in [33, 35, 36, 37].

### III. MECHANICAL DESIGN OF THE VISIFLEX

The Visiflex consists of three main elements: (1) the fingertip, consisting of an acrylic dome, a silicone cap, an LED board, and a 3D-printed enclosure; (2) a 6-dof flexure; and (3) the base, which consists of a compact camera with a wide-angle lens and a custom enclosure. We define a camera frame  $\{c\}$  fixed to the base, a dome frame  $\{d\}$  fixed to the fingertip at the center of the hemispherical dome, and a frame  $\{r\}$ , fixed relative to  $\{c\}$ , that coincides with  $\{d\}$  when the flexure is relaxed, i.e., no wrench is transmitted through it (Figure 2). Without loss of generality, we assume that  $\{c\}$  is stationary, and it serves as the frame in which contact locations and contact wrenches are reported. The configuration of  $\{r\}$  relative to  $\{c\}$  is a constant  $T_{cr} \in SE(3)$ , and the configuration of the frame  $\{d\}$  relative to  $\{c\}$  is written  $T_{cd}$ .

#### A. Fingertip

The inner rigid dome of the fingertip is made of acrylic plastic. The outer cap is molded out of opaque silicone rubber infused with fluorescent yellow dye (Mold Start 20T Silicone with Silc-Pig silicone pigment). The concept for the flexible cap is taken from [12], but our cap is molded to have small bumps on the inner surface, which are normally lightly pressed against the acrylic waveguide. These bumps ensure a consistent gap everywhere between the cap and the dome. This design also eliminates mechanical deadband in detecting contact, as is present in designs with an airgap between the cap and the dome (e.g., [12]).

A custom PCB ring is located at the base of the dome. Eight downward-facing red LED fiducials allow the camera to

track the motion of the fingertip. Upward-facing blue LEDs infuse blue light into the dome waveguide. This light is totally internally reflected within the dome, except at points of contact with the cap, where green light (due to the blue LEDs and fluorescent yellow cap interior) scatters inward toward the camera due to FTIR. Bright spots are registered as contact points on the dome.

#### B. 6-dof Flexure

The flexure assembly consists of a rigid body at its proximal end (at the base of the Visiflex), fixed relative to  $\{c\}$ ; a rigid body at its distal end (at the fingertip), fixed relative to  $\{d\}$ ; and the flexure in between. We assume that no forces are applied to the flexure between the proximal and distal ends. We define  $\{f\}$  to be a frame fixed relative to the distal end when the flexure is relaxed, i.e., supporting no forces or torques. (One candidate for  $\{f\}$  is  $\{r\}$ , but other choices are possible.) Let  $\{f'\}$  be the frame when the flexure is displaced, and  $T_{ff'} = \exp(\mathcal{X}_f) \in SE(3)$  be the representation of  $\{f'\}$  relative to  $\{f\}$ , where  $\mathcal{X}_f = (\omega_x, \omega_y, \omega_z, v_x, v_y, v_z)$  is a 6-vector of exponential coordinates [38].

The 6-vector wrench applied to the distal end of the flexure is expressed relative to the frame  $\{f\}$  as  $\mathcal{F}_f = (m_x, m_y, m_z, f_x, f_y, f_z)$ , a vector of three moments and three forces. In the ideal case,  $\mathcal{F}_f$  can be expressed as

$$\mathcal{F}_f = \mathcal{K}_f(\mathcal{X}_f), \quad (1)$$

i.e.,  $\mathcal{K}_f$  is a function only of the current displacement  $\mathcal{X}_f$ . This assumption relies on the flexure having low hysteresis, stress relaxation, and creep, and in cases where the fingertip velocity and acceleration are non-negligible, low viscosity and mass. We also require that the flexure be capable of significant deformation without plastically deforming and that the design avoid stress concentrations and mechanical fatigue. For these reasons, we construct our flexures out of spring steel, stainless steel, or related highly-resilient metals.<sup>2</sup>

The linearized approximation to Equation (1) about the relaxed configuration, valid when the displacement  $\mathcal{X}_f$  is small, is

$$\mathcal{F}_f = K_f \mathcal{X}_f, \quad (2)$$

where  $K_f$  is a  $6 \times 6$  symmetric positive-definite stiffness matrix. The 36-element stiffness matrix has up to 21 unique entries: the six elements along the diagonal and the 15 elements in the upper-right triangle, since the 15 elements in the lower-left triangle are defined by symmetry.

Given the stiffness matrix in the frame  $\{f\}$ , the stiffness expressed in any other frame  $\{a\}$  is

$$K_a = [\text{Ad}_{T_{af}}]^{-T} K_f [\text{Ad}_{T_{af}}]^{-1} \quad (3)$$

where  $[\text{Ad}_{T_{af}}]$  is the  $6 \times 6$  matrix adjoint representation of the transformation matrix  $T_{af}$  [38].

<sup>2</sup>3D-printed flexures have also been tested, but most 3D-printed materials exhibit poor hysteresis, stress relaxation, and creep properties. In this case, we could either accept the significant errors that come from the non-ideal properties of the material, or we could attempt to model, or learn a model from data, the transmitted wrench based on the full time history  $\mathcal{X}(t)$ , essentially trying to correct the mechanical design with software.

The 6-dof flexure should be swappable based on the robot or the task. Our first application is in-hand sliding regrasp with the Allegro hand, and each fingertip can generate approximately 10 N of force in any direction at a typical configuration. Based on the dimensions of the fingertip, the maximum linear deflection of the flexure should be on the order of 2-4 mm. Hence our target stiffness in each of the three linear axes is in the range 2.5-5 N/mm.

Therefore an appropriate target stiffness matrix is

$$K_f = \begin{bmatrix} k_{\omega_x} & 0 & 0 & 0 & 0 & 0 \\ 0 & k_{\omega_y} & 0 & 0 & 0 & 0 \\ 0 & 0 & k_{\omega_z} & 0 & 0 & 0 \\ 0 & 0 & 0 & 4000 \text{ N/m} & 0 & 0 \\ 0 & 0 & 0 & 0 & 4000 \text{ N/m} & 0 \\ 0 & 0 & 0 & 0 & 0 & 4000 \text{ N/m} \end{bmatrix},$$

where the rotational stiffnesses are not critical for the application of in-hand manipulation with the Allegro hand.

Desired stiffness properties can be achieved by fabricating a fully custom flexure or by using one or more commercially-available flexures. For example, using three or more springs as “legs” in a parallel mechanism can provide enough geometric and spring parameters to provide access to a full-dimensional subset of the 21-dimensional space of linear stiffness matrices. For simplicity of assembly in the current Visiflex, however, we use a single commercial compression spring as our 6-dof flexure (Figure 1). Advantages of compression springs are that they are inexpensive, readily available in many configurations, and stresses are relatively evenly distributed over the spring’s length, resulting in significant elastic deformability and little fatigue.

Compression springs are typically chosen for their stiffness in a single direction, but they also exhibit finite stiffness in other directions. In addition to material properties, four design parameters for a typical compression spring (wire radius, mean diameter of the spring, the pitch of the spring, and the number of coils) allow tuning of the stiffness matrix in a four-dimensional space, including limited adjustment of the relative rotational and translational stiffness. When choosing the spring’s parameters, inequality constraints imposed by the overall size of the fingertip and avoiding camera occlusion must also be taken into account.

Building on the work in [39] and [40], we derived a closed-form approximation to the  $6 \times 6$  stiffness matrix of a compression spring, valid in the limiting case of zero pitch and a large number of coils. In the current Visiflex prototype, the flexure is a stainless steel 302 ASTM A313 compression spring with a rest length of 19.8 mm, a wire radius of 2.03 mm, a mean diameter of 27.73 mm, a pitch angle of 0.1029 radians, and 3.75 coils. Choosing  $\{f\}$  at the center of the spring with its  $\hat{z}$ -axis along the center line of the spring, the theoretical stiffness (in SI units) is

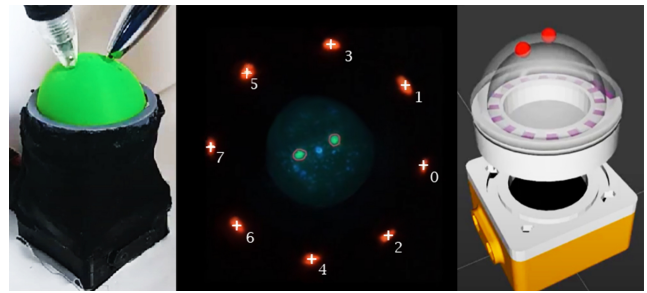


Fig. 3: (Left) The Visiflex is contacted at two points. (Middle) Camera image showing the extracted locations of the fiducials and the contacts. (Right) The fingertip dome configuration and contact points visualized in rviz.

$$K_f = \begin{bmatrix} 0.88 & 0 & 0 & 0 & 0 & 0 \\ 0 & 0.88 & 0 & 0 & 0 & 0 \\ 0 & 0 & 1.06 & 0 & 0 & 0 \\ 0 & 0 & 0 & 10913 & 0 & 0 \\ 0 & 0 & 0 & 0 & 10913 & 0 \\ 0 & 0 & 0 & 0 & 0 & 3911 \end{bmatrix},$$

which meets our target stiffness in the  $\hat{z}$  direction and is about 2.5 times our target stiffness in the other linear directions. Representing the stiffness in the camera frame  $\{c\}$ , we get

$$K_c = \begin{bmatrix} 2.22 & 0 & 0 & 0 & -121 & 0 \\ 0 & 2.22 & 0 & 121 & 0 & 0 \\ 0 & 0 & 1.0 & 0 & 0 & 0 \\ 0 & 121 & 0 & 10913 & 0 & 0 \\ -121 & 0 & 0 & 0 & 10913 & 0 \\ 0 & 0 & 0 & 0 & 0 & 3911 \end{bmatrix}.$$

### C. Camera and Lens

Criteria for the Visiflex camera and lens include high resolution, compact form factor, low cost, a wide field of view, and a depth of field such that all fiducials and contacts have acceptable sharpness.

Based on these considerations, we chose the Basler Dart daA1600-60uc color camera [41] (60 fps,  $1600 \times 1200$  pixels) and a  $165^\circ$  fisheye lens. Standard camera calibration is used to account for the distortion of the wide-angle lens. Based on the camera optics and the geometry of the Visiflex, direct imaging of a 1 mm horizontal motion of one of the LED fiducials yields approximately 30 pixels of motion in the CMOS imager.

Figure 3 shows an example camera image and the result of software processing (Section IV). The tracked motion of the red fiducials is translated into a pose estimate for the dome, and any green spots are interpreted as contact points on the dome.

## IV. SOFTWARE

The Visiflex sensor uses OpenCV [42] to parse the data stream from the camera into the position and orientation of the fingertip and contact locations on the fingertip. In this

paper, results are reported for a Lenovo Y700 laptop with a Core i7-6700 CPU @ 2.6 GHz and 16 GB RAM running Ubuntu 14.04. Frames are processed at 40 Hz on three parallel cores: one to handle camera input, one for fiducial tracking and fingertip pose estimation, and one for contact detection.

#### A. Fiducial Tracking and Fingertip Pose Estimation

Tracking  $T_{cd}$ , the position and orientation of the fingertip dome frame  $\{d\}$  relative to the camera frame  $\{c\}$ , is an example of the Perspective- $n$ -Point (PnP) problem in computer vision: given a calibrated camera,  $n \geq 3$  points at fixed locations on a known rigid body (the dome), and the corresponding  $n$  points in the camera's image, determine the position and orientation of the rigid body relative to the camera frame. For the Visiflex,  $n = 8$ , the red LED fiducials on the underside of the LED PCB ring. The red fiducials are color-space separated from the FTIR images of the contacts and their centroids are tracked at 40 Hz as the dome moves. To solve the PnP problem we use OpenCV's `solvePnP` function, based on the algorithm described in [43].

#### B. Contact Detection and Localization

Images of contact points due to FTIR appear as green to the camera. These green blobs are color-space separated from the fiducials and size-filtered (to eliminate small signals due to the bumps on the silicone cap contacting the waveguide), and the centroids of the remaining blobs correspond to actual contacts.

Each centroid in the image corresponds to a fixed ray relative to the camera frame  $\{c\}$ , as determined by the calibration of the camera and fish-eye lens. The intersections of a line along this ray with a sphere centered at the origin of  $\{d\}$  (obtained from  $T_{cd}$  from fiducial tracking in Section IV-A) are given by the solutions of a quadratic equation, and the solution farthest from  $\{c\}$  corresponds to the actual contact point.

Because the fingertip is strictly convex, contacts with hard objects that are locally flat or convex result in small convex contact patches. If objects are soft or concave, however, other types of contact patches (and images) are possible, and the camera software can be modified to extract other types of contact geometry. In this paper we focus on the precision and accuracy of point contact location detection, as this is relevant to the accuracy of reconstructing any contact geometry.

#### C. Wrench Sensing

Given  $T_{cd}$  from fiducial tracking and the constant  $T_{cr}$ , we define  $[\mathcal{X}_c] = \log(T_{cd}T_{cr}^{-1}) \in se(3)$ , where  $\mathcal{X}_c = (\omega_c, v_c) \in \mathbb{R}^6$  are the exponential coordinates, expressed in  $\{c\}$ , describing the configuration of the frame  $\{d\}$  relative to  $\{r\}$ . If the flexure is at its rest configuration,  $\mathcal{X}_c = 0$ .

We explore two techniques to estimate the wrench  $\mathcal{F}_c$  from the measured dome configuration  $\mathcal{X}_c$ : (1) using an estimated stiffness matrix  $K_c$  (i.e.,  $\mathcal{F}_c = K_c\mathcal{X}_c$ ) under the assumption of small displacements of the dome or a globally linear relationship between  $\mathcal{F}_c$  and  $\mathcal{X}_c$ ; and (2) fitting general nonlinear function approximators  $\mathcal{F}_c = \mathcal{K}_c(\mathcal{X}_c)$  to the experimental data, e.g., based on local linear regression or neural networks.

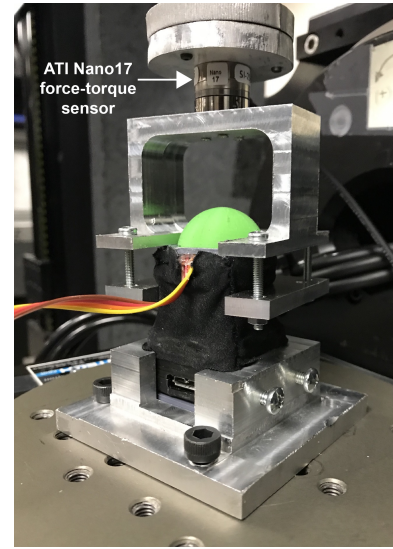


Fig. 4: The Visiflex sensor mounted in the 5-dof LIPMM testing machine. The Visiflex is fixed to the baseplate, a custom clamp holds the dome, and an ATI Nano17 force-torque sensor connects the clamp to the LIPMM.

## V. EXPERIMENTAL VALIDATION

We experimentally characterized the performance of the Visiflex in terms of its accuracy in estimating the pose of the fingertip dome, accuracy of wrench sensing, and accuracy of contact location sensing. For the first two, we used a custom five-degree-of-freedom (three translational dofs and two rotational dofs) testing rig called the LIPMM, named for its primary use in laser-induced plasma micromachining (Figure 4). The repeatability of the LIPMM's positioning is approximately  $1 \mu\text{m}$  in linear motion and  $0.001^\circ$  in rotation.

The LIPMM was used to create precise displacements of the fingertip dome relative to the Visiflex base. An ATI Nano17 force-torque sensor was used to measure the actual wrenches applied to the fingertip.

#### A. Pose Estimation

The fingertip dome was moved to 265 random poses in a range of 1 mm along the  $\hat{x}_c$  and  $\hat{y}_c$  axes and 4 mm along the  $\hat{z}_c$  axis. Each point was visited twice. The LIPMM's displacement was taken as ground truth. For each test point, the Visiflex's error was calculated as the difference between the Visiflex's fiducial-tracking estimate of the displacement of the dome along the three linear axes compared to the ground truth. Figure 5 displays a box plot of the error along each axis. The average absolute error in the dome pose estimate was around  $20 \mu\text{m}$ , the maximum error in the  $\hat{x}_c$  and  $\hat{y}_c$  directions was less than  $100 \mu\text{m}$ , and the maximum error in the  $\hat{z}_c$  direction was less than  $300 \mu\text{m}$ .

#### B. Wrench Sensing

##### 1) Nonideal Behavior: Stress Relaxation and Hysteresis:

A metal flexure was chosen to minimize stress relaxation, which is the phenomenon of decreasing stress in a structure

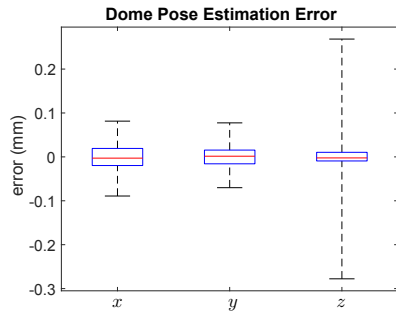


Fig. 5: Error between the fiducial-tracking vision-based estimation of the dome’s displacement (along three linear axes) and the actual displacement generated by the LIPMM when it moves in a point cloud of arbitrary poses. The box plots indicate the minimum error, maximum error, and the 25, 50, and 75 percentile error.

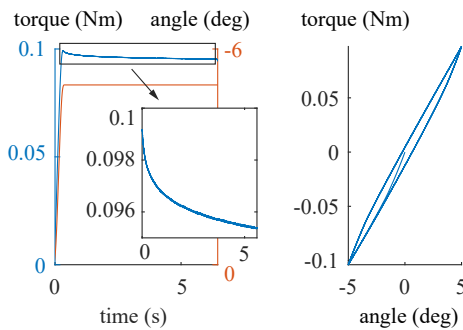


Fig. 6: (Left) Torque relaxation for rotation about the  $\hat{z}_c$  axis. The inset magnifies the relaxing torque. (Right) Hysteresis for rotation about the  $\hat{z}_c$  axis.

over time in response to a constant strain, and hysteresis, the phenomenon that stress depends on the history of motion, not just the current strain. Nonetheless, the Visiflex includes 3D-printed PLA housings and epoxy interfaces between the housings and the flexure, which create opportunities for non-ideal behavior in the stress-strain properties.

For the stress relaxation tests, we imposed a step displacement along the five principal axes of motion of the LIPMM and collected force-torque data at 1000 Hz for six seconds. Figure 6 (left) shows a representative result, for rotation about the  $\hat{z}_c$  axis and torques measured about the same axis. While some stress relaxation is apparent, it is small, and these results are typical of all five axes tested. Measured changes in forces or torques were less than 4% over the measurement timeframe for all five axes, approximately following a first-order decay.

For hysteresis testing, the LIPMM again was moved along its five axes in small increments, beginning from zero and cycling between a maximum positive displacement along the axis to a maximum negative displacement. Figure 6 (right) shows a typical hysteresis loop, expressed as torque about the  $\hat{z}_c$  axis vs. rotation angle about the  $\hat{z}_c$  axis. Typical results for each axis show a maximum error of 2-5% of the full range of force/torque magnitudes compared to the median value of the

force/torque reading at each angle.

These nonideal effects are relatively small, but in a future version of the LIPMM we will investigate further decreasing them through the design of the dome and base housings and their interface to the flexure.

2) *Estimated Stiffness Matrix*: We used the data from the hysteresis experiments, augmented with virtual “mirrored” data in the direction not tested by the 5-dof LIPMM (i.e., an assumption of symmetry), to fit a stiffness matrix  $K_c$  at the relaxed configuration. We solve for the 21 upper-triangular entries of  $K_c$  that best fit

$$[\mathcal{F}_{c1} \mathcal{F}_{c2} \dots \mathcal{F}_{ck}] = K_c[\mathcal{X}_{c1} \mathcal{X}_{c2} \dots \mathcal{X}_{ck}]$$

in the least-squares sense, where  $\{\mathcal{F}_{ci}, \mathcal{X}_{ci}\}$  is a single experimental data point.

The results are mirrored about the diagonal of  $K$ , since the stiffness matrix must be symmetric. The result is

$$K_c = \begin{bmatrix} 1.56 & 0.03 & -0.05 & -2.22 & -37.8 & 11.00 \\ 0.03 & 1.48 & -0.05 & 30.1 & 7.84 & 19.80 \\ -0.05 & -0.05 & 1.09 & -7.51 & 4.46 & 1.39 \\ -2.22 & 30.06 & -7.51 & 5830 & -274 & 255 \\ -37.81 & -7.84 & 4.46 & -274 & 6586 & 622 \\ 11.00 & 19.80 & 1.39 & 255 & 622 & 4177 \end{bmatrix}$$

As with the theoretical prediction in Section III-B, the terms along the diagonals of the top left and bottom right  $3 \times 3$  submatrices dominate the off-diagonal terms. The linear stiffness in the  $\hat{z}_c$  direction approximately matches the theoretical prediction of 3911 N/m. Linear stiffness along, and rotational stiffness about, the  $\hat{x}_c$  and  $\hat{y}_c$  axes do not match as closely. This is likely due to the approximations used in the closed-form theoretical model (e.g., zero pitch and a large number of active coils).

3) *Force Sensing*: To characterize the performance of the Visiflex as a force sensor for general dome displacements, not just small displacements, we used experimental data to fit a function  $\mathcal{K}_c$  satisfying  $\mathcal{F}_c = \mathcal{K}_c(\mathcal{X}_c)$ . The LIPMM and the Visiflex were used to collect 502 data points of the form  $\{\mathcal{X}_{est}, \mathcal{X}_c, \mathcal{F}_c\}$ , where  $\mathcal{X}_{est}$  was the estimated dome pose from the Visiflex vision system,  $\mathcal{X}_c$  was the actual dome pose controlled by the LIPMM (chosen randomly within the workspace of the Visiflex), and  $\mathcal{F}_c$  was the actual wrench on the fingertip as reported by the ATI force-torque sensor (expressed in the camera frame  $\{c\}$ ). Of the 502 data points, 92 pairs of the form  $\{\mathcal{X}_c, \mathcal{F}_c\}$  were used to construct the model  $\mathcal{K}_c$ , and the  $\{\mathcal{X}_{est}, \mathcal{F}_c\}$  values from the remaining 410 data points were used to test the wrench-sensing performance of the Visiflex. For each test point, the wrench estimated by the Visiflex was  $\mathcal{F}_{est} = \mathcal{K}_c(\mathcal{X}_{est})$  and the estimated wrench error was  $\mathcal{F}_e = \mathcal{F}_c - \mathcal{F}_{est}$ .

We experimented with multiple general nonlinear functional representations of  $\mathcal{K}_c$ , including weighted interpolation of nearby experimental data, but we found that a global linear model fit using least-squares yielded comparable results for our test displacements. The force-sensing accuracy is reported in Table I for the three linear forces. The average errors in the linear force estimates are quite small, but the standard deviations are approximately 0.3 N.

TABLE I: Force Sensing Accuracy

Axis	Average error (N)	Standard deviation (N)
$\hat{x}_c$	0.07473	0.30461
$\hat{y}_c$	-0.06030	0.29745
$\hat{z}_c$	-0.07051	0.33911

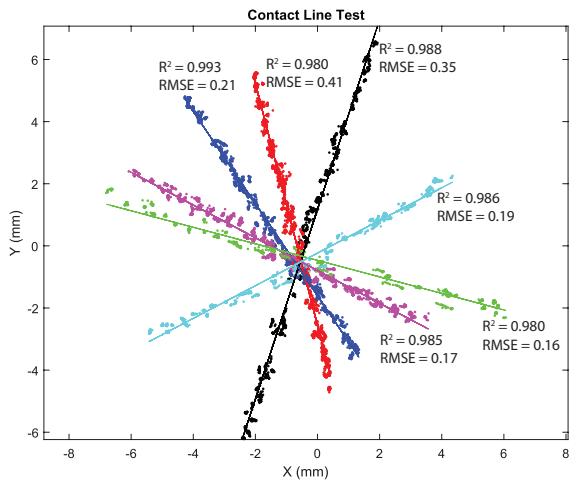


Fig. 7: Results of contact location linearity tests. Note the high  $R^2$  values of the linear fits and the small RMSE values.

### C. Contact Location Sensing

To test the accuracy of localizing contact points, we placed rigid testing caps over the Visiflex fingertip to allow testing of precise contact locations. One rigid cap features a slit opening (test 1, Section V-C1), while the other has 17 discrete holes (test 2, Section V-C2). A blunted crafting needle was used to poke the Visiflex through the slit or holes of the testing caps, allowing contacts along the intersection of a vertical plane with the dome (test 1) and at specific points (test 2).

1) *Test 1: Contacts in a Plane:* Figure 7 shows the reported  $(x_c, y_c)$  contact locations on the dome when the test cap slit opening was oriented at six randomly chosen orientations. For each orientation, the Visiflex was poked at least 50 times along the slit. These contacts should lie along a line in the  $(x_c, y_c)$  plane, and the fitted lines match the data closely, with all  $R^2$  values in excess of 0.98 and root mean square errors of less than 0.5 mm. This can be compared to the 1.25 mm width of the slit, which allows a positioning variability of the needle within the slit of approximately 0.5 mm.

2) *Test 2: Contact Point Localization:* Figure 8 shows the results of collecting 200 data points at each of the 17 contact locations. The measured contacts are tightly bunched, with an average standard deviation of 0.045 mm and an average spatial error from the cap hole locations of 0.71 mm.

## VI. CONCLUSION

The Visiflex is an inexpensive compliant tactile fingertip, capable of measuring the contact wrench and multiple contact locations at 40 Hz, while also providing consistent compliance appropriate for manipulation of rigid objects.

We are currently duplicating the sensor for the four fingers of the Allegro hand. Figure 9 shows the current sensor

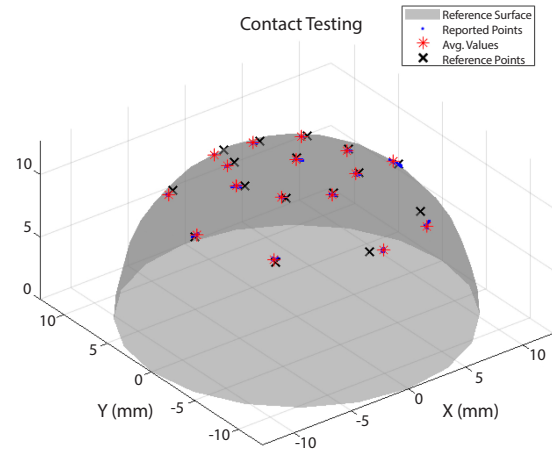


Fig. 8: Comparison of detected contact points on the dome with the reference points. Accuracy is slightly worse near the edges, perhaps due in part to the reduced camera resolution near the boundaries of the dome.

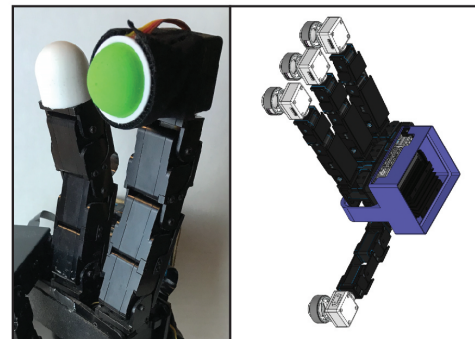


Fig. 9: (Left) The prototype attached to a single finger of the Allegro hand. (Right) A CAD rendering of four fingers of the Allegro hand equipped with Visiflex tactile fingertips. An NVIDIA Jetson Nano board mounted to the back of the hand is for vision processing.

mounted to an Allegro finger and a CAD model of four sensors and an NVIDIA Jetson Nano board mounted to the back of the hand for vision processing. Our initial results show that the Jetson Nano can process at least 100 frames per second, and our next step is to optimize the software to maximize the processing rate of the four tactile sensors (up to a maximum of 60 Hz each). The well-characterized stiffness and contact force and location measurement provided by the Visiflex fingertips match the requirements for control of quasistatic in-hand sliding regrasps in [2], and our future work will focus on robust implementation of in-hand sliding manipulation using the Visiflex fingertips.

## REFERENCES

- [1] J. Shi, J. Z. Woodruff, P. B. Umbanhowar, and K. M. Lynch, "Dynamic in-hand sliding manipulation," *IEEE Transactions on Robotics*, vol. 33, no. 4, pp. 778–795, Aug 2017.
- [2] J. Shi, H. Weng, and K. M. Lynch, "In-hand sliding regrasp with spring-sliding compliance and external constraints," *IEEE Access*, vol. 8, pp. 88 729–88 744, Apr. 2020.

- [3] “Tactileglove by pressure profile systems,” <https://pressureprofile.com/about/tactile-sensing>.
- [4] A. Charalambides and S. Bergbreiter, “Rapid manufacturing of mechanoreceptive skins for slip detection in robotic grasping,” *Advanced Materials Technologies*, vol. 2, p. 1600188, 2017.
- [5] “SynTouch BioTac tactile sensor,” <https://www.syntouchinc.com/en/sensor-technology/>.
- [6] T. Hellebrekers, O. Kroemer, and C. Majidi, “Soft magnetic skin for continuous deformation sensing,” *Advanced Intelligent Systems*, vol. 1, no. 4, p. 1900025, 2019.
- [7] S. Omata and Y. Terunuma, “New tactile sensor like the human hand and its applications,” *Sensors and Actuators A: Physical*, vol. 35, no. 1, pp. 9–15, 1992.
- [8] J.-S. Heo, J.-H. Chung, and J.-J. Lee, “Tactile sensor arrays using fiber Bragg grating sensors,” *Sensors and Actuators A: Physical*, vol. 126, no. 2, pp. 312–327, 2006.
- [9] R. S. Dahiya, G. Metta, M. Valle, and G. Sandini, “Tactile sensing: from humans to humanoids,” *IEEE Transactions on Robotics*, vol. 26, no. 1, pp. 1–20, 2010.
- [10] Z. Kappassov, J.-A. Corrles, and V. Perdereau, “Tactile sensing in dexterous robot hands – review,” *Robotics and Autonomous Systems*, vol. 74, pp. 195–220, 2015.
- [11] S. Begej, “Planar and finger-shaped optical tactile sensors for robotic applications,” *IEEE Journal on Robotics and Automation*, vol. 4, no. 5, pp. 472–484, 1988.
- [12] H. Maekawa, K. Tanie, K. Komoriya, M. Kaneko, C. Horiguchi, and T. Sugawara, “Development of a finger-shaped tactile sensor and its evaluation by active touch,” in *Proceedings 1992 IEEE International Conference on Robotics and Automation*, May 1992, pp. 1327–1334 vol.2.
- [13] K. M. Lynch, H. Maekawa, and K. Tanie, “Manipulation and active sensing by pushing using tactile feedback,” in *IEEE/RSJ International Conference on Intelligent Robots and Systems*, Raleigh, NC, 1992, pp. 416–421.
- [14] B. Ward-Cherrier, N. Pestell, L. Cramphorn, B. Winstone, M. E. Giannaccini, J. Rossiter, and N. F. Lepora, “The TacTip family: soft optical tactile sensors with 3D-printed biomimetic morphologies,” *Soft Robotics*, vol. 5, no. 2, pp. 216–227, 2018.
- [15] A. Yamaguchi and C. G. Atkeson, “Implementing tactile behaviors using FingerVision,” in *IEEE International Conference on Humanoid Robotics*, 2017.
- [16] W. Yuan, S. Dong, and E. H. Adelson, “Gelsight: High-resolution robot tactile sensors for estimating geometry and force,” *Sensors*, vol. 17, no. 12, p. 2762, 2017.
- [17] M. Lambeta, P.-W. Chou, S. Tian, B. Yang, B. Maloon, V. R. Most, D. Stroud, R. Santos, A. Byagowi, G. Kammerer, D. Jayaraman, and R. Calandra, “DIGIT: A novel design for a low-cost compact high-resolution tactile sensor with application to in-hand manipulation,” *IEEE Robotics and Automation Letters*, vol. 5, no. 3, p. 3838–3845, Jul 2020.
- [18] A. Padmanabha, F. Ebert, S. Tian, R. Calandra, C. Finn, and S. Levine, “OmniTact: A multi-directional high resolution touch sensor,” 2020, arXiv cs.RO.
- [19] A. Tar and G. Cserey, “Development of a low cost 3d optical compliant tactile force sensor,” in *2011 IEEE/ASME International Conference on Advanced Intelligent Mechatronics (AIM)*. IEEE, 2011, pp. 236–240.
- [20] P. Piacenza, K. Behrman, B. Schifferer, I. Kymissis, and M. Ciocarlie, “A sensorized multicurved robot finger with data-driven touch sensing via overlapping light signals,” *IEEE/ASME Transactions on Mechatronics*, pp. 1–1, 2020.
- [21] R. Ouyang and R. Howe, “Low-cost fiducial-based 6-axis force-torque sensor,” in *IEEE International Conference on Robotics and Automation*, 2020.
- [22] W. Li, A. Alomainy, I. Vitanov, Y. Noh, P. Qi, and K. Althofer, “F-TOUCH sensor: Concurrent geometry perception and multi-axis force measurement,” *IEEE Sensors*, Oct. 2020.
- [23] L. L. Howell, *Compliant mechanisms*. John Wiley & Sons, 2001.
- [24] F. Wang, C. Liang, Y. Tian, X. Zhao, and D. Zhang, “Design and control of a compliant microgripper with a large amplification ratio for high-speed micro manipulation,” *IEEE/ASME Transactions on Mechatronics*, vol. 21, no. 3, pp. 1262–1271, 2016.
- [25] L. Rubbert, S. Caro, J. Gangloff, and P. Renaud, “Using singularities of parallel manipulators to enhance the rigid-body replacement design method of compliant mechanisms,” *Journal of Mechanical Design*, vol. 136, no. 5, p. 051010, 2014.
- [26] D. Rollinson, S. Ford, B. Brown, and H. Choset, “Design and modeling of a series elastic element for snake robots,” in *ASME 2013 Dynamic Systems and Control Conference*. American Society of Mechanical Engineers, 2013.
- [27] E. Baker, T. Reissman, F. Zhou, C. Wang, K. Lynch, and C. Sun, “Microstereolithography of three-dimensional polymeric springs for vibration energy harvesting,” *Smart Materials Research*, 2012.
- [28] J. B. Hopkins and M. L. Culpepper, “Synthesis of multi-degree of freedom, parallel flexure system concepts via freedom and constraint topology (FACT) Part I: Principles,” *Precision Engineering*, vol. 34, no. 2, pp. 259–270, 2010.
- [29] —, “Synthesis of multi-degree of freedom, parallel flexure system concepts via freedom and constraint topology (FACT) Part II: Practice,” *Precision Engineering*, vol. 34, no. 2, pp. 271–278, 2010.
- [30] L. L. Howell, S. P. Magleby, and B. M. Olsen, *Handbook of Compliant Mechanisms*, ser. A Wiley-Interscience publication. Wiley, 2013.
- [31] M. A. Pucheta and A. Cardona, “Design of bistable compliant mechanisms using precision–position and rigid-body replacement methods,” *Mechanism and Machine Theory*, vol. 45, no. 2, pp. 304–326, 2010.
- [32] J. Deng, K. Rorschach, E. Baker, C. Sun, and W. Chen, “Topology optimization and fabrication of low frequency vibration energy harvesting microdevices,” *Smart Materials and Structures*, vol. 24, no. 2, p. 025005, 2014.
- [33] M. Y. Wang and S. Chen, “Compliant mechanism optimization: analysis and design with intrinsic characteristic stiffness,” *Mechanics Based Design of Structures and Machines*, vol. 37, no. 2, pp. 183–200, 2009.
- [34] M. Y. Wang, X. Wang, and D. Guo, “A level set method for structural topology optimization,” *Computer Methods in Applied Mechanics and Engineering*, vol. 192, no. 1-2, pp. 227–246, 2003.
- [35] C. J. Kim, Y.-M. Moon, and S. Kota, “A building block approach to the conceptual synthesis of compliant mechanisms utilizing compliance and stiffness ellipsoids,” *Journal of Mechanical Design*, vol. 130, no. 2, p. 022308, 2008.
- [36] D. J. Cappelleri, G. Krishnan, C. Kim, V. Kumar, and S. Kota, “Toward the design of a decoupled, two-dimensional, vision-based  $\mu$ n force sensor,” *Journal of Mechanisms and Robotics*, vol. 2, no. 2, p. 021010, 2010.
- [37] G. Krishnan, C. Kim, and S. Kota, “An intrinsic geometric framework for the building block synthesis of single point compliant mechanisms,” *Journal of Mechanisms and Robotics*, vol. 3, no. 1, 2011.
- [38] K. M. Lynch and F. C. Park, *Modern Robotics*. Cambridge University Press, 2017.
- [39] L. Lindkvist, *Three-dimensional load-deformation relationships of arbitrarily loaded coiled springs*. Chalmers University of Technology, 1995.
- [40] J. Potratz, J. Yang, K. Abdel-Malek, E. P. Pitarch, and N. Grosland, “A light weight compliant hand mechanism with high degrees of freedom,” vol. 127, no. 6, pp. 934–945, Nov. 2005.
- [41] “Basler dart daa1600-60uc camera,” [www.baslerweb.com](http://www.baslerweb.com).
- [42] “OpenCV computer vision library,” <https://opencv.org/>.
- [43] V. Lepetit, F. Moreno-Noguer, and P. Fua, “EPnP: An accurate  $o(n)$  solution to the PnP problem,” *International Journal of Computer Vision*, vol. 81, pp. 155–166, 2009.